


# Detecting Unmodeled, Source-Dependent Signals in Gravitational Waves with SCoRe

Guillaume Dideron <sup>\*</sup>

*Department of Physics and Astronomy, University of Waterloo,  
200 University Avenue West, Waterloo, ON N2L 3G1, Canada and  
Perimeter Institute for Theoretical Physics, 31 Caroline Street North, Waterloo, ON N2L 2Y5, Canada*

Suvodip Mukherjee <sup>†</sup>

*Department of Astronomy & Astrophysics, Tata Institute of Fundamental Research,  
1, Homi Bhabha Road, Colaba, Mumbai 400005, India*

Luis Lehner <sup>‡</sup>

*Perimeter Institute for Theoretical Physics, 31 Caroline Street North, Waterloo, ON N2L 2Y5, Canada  
(Dated: November 8, 2024)*

New physics and systematic errors can lead to deviations between the models used to analyze gravitational wave data and the actual signal. Such deviations will generally be correlated between detectors and manifest differently across the gravitational wave source parameter space. The previously introduced SCoRe framework uses these features to distinguish these deviations from noise and extract physical information from their source-dependent variation. In this work, we further analyze the hierarchical component of the method—we include the expected dependence of the deviations on the source parameters into the inference process, obtaining more physically informative results. As a specific example, we study a deviation that scales as a power law of the mass scale of black hole binaries—as, for example, in Effective Field Theory of gravity. We show how the signal-to-noise ratio of the cross-correlated residual power can be used to recover the power-law index. We demonstrate how both the distribution in source and deviation strength determine which region of source parameter space influences the inference most. Finally, we forecast the constraint on the power law index for a network of two Cosmic Explorer-like detectors with a year of observation period.

## I. INTRODUCTION

Gravitational Waves (GWs) give us a window to an otherwise invisible side of the universe. The first three observation runs of Advanced LIGO [1], Advanced Virgo [2], and KAGRA [3–5] have allowed the study of a wide range of phenomena, in cosmology, astrophysics, and fundamental physics (see, e.g. [1, 2, 6–12]). At the core of these efforts, the inference of physical information from GWs relies on our understanding of the emission mechanism, the sources of GWs, and the noise in the detectors. These assumptions we dub the Standard Model (SM) of GWs. The SM is used to compute waveform models of the signal from a target source<sup>1</sup>. These waveform models generally have finite precision, and may not fully implement known physics (such as overlapping signals, eccentricity, dynamical tides, etc), and most omit yet unknown physics (such as deviations from General Relativity (GR) or alternative compact objects). Such mismodeling gives rise to a difference between the physical signal in the data and the SM waveforms. We term

such differences Beyond Modeled (BM) signatures. The presence of new physics in the data [8] as well as the impact of systematic errors on parameter estimation [19, 20] and on the detection of new physics [21] are regularly studied, and SM waveforms are continuously improved.

Next generation GW detectors (in the  $\approx [1 - 10^4]$  Hz window) such as Cosmic Explorer (CE) [22] and the Einstein Telescope [23], are expected to detect events with maximum Signal-to-Noise Ratios (SNRs) on the order of  $\mathcal{O}(10^3)$  and at rates in the order of  $\mathcal{O}(10^5)\text{yr}^{-1}$  [24, 25]. As a comparison, the  $\sim 90$  confident events currently in the third Gravitational-Waves Transient Catalogs have maximum SNRs on the order  $\mathcal{O}(10^1)$  [26–29]. This increase in performance means that BM signatures will likely become more significant compared to random noise. Without a proper grasp of their effect and origin, we may miss new physical effects or create biases in our analyses [30]. Options to address this shortcoming have been presented and improved in multiple techniques. For instance, BM signatures may be detected in a data-driven way through the residual test used, for example, in [8, 31–33].

An important feature of BM signatures is that they can vary across events with the GW source properties such as mass, spin, eccentricity, etcetera.

We believe this point has so far not yet been fully exploited in the analysis of GW data. This has been studied, for example, in [34–40]. In this work, we explore the inclusion of the source parameter dependence of BM signatures in SCoRe [41], a method to detect and extract BM

<sup>\*</sup> gdidiron@perimeterinstitute.ca

<sup>†</sup> suvodip@tifr.res.in

<sup>‡</sup> llehner@perimeterinstitute.ca

<sup>1</sup> Note that the detection of GWs itself does not require models. For example, the coherent WaveBurst [13–17] pipeline identifies excess power that is coherent across detectors and has been used in LVK analyses, and the MLy [18] pipeline uses convolution neural networks to identify coherent signals between detectors.

signatures with minimal assumptions on their form by using the residual power left after subtracting the model from the data. In brief, the method has 3 steps: (1) The cross-correlated residual power in pairs of detectors is computed to reduce the effect of uncorrelated noise. (2) That power is filtered for physically motivated behavior. (3) Information from different events is combined to inform on the origin of the BM signature. In this work, after briefly reviewing the formalism underlying **SCoRe**, we further elaborate on the method's third step. We demonstrate that the dependence of a BM deviation on source parameters can be recovered with the method, and forecast the constraints on SM deviations from GW events by a two CE-like detector network over a year. The residual test mentioned above uses the *BayesWave* method to identify any excess residual power in the detectors by fitting wavelets data to coherent signal [42–45]. Instead, the **SCoRe** method takes the cross-correlation between detectors and compliments the residual test by looking for specific morphology in the residual power and/or the correlation of the residual with source properties.

This work is organized as follows: In Sec. II, we describe the **SCoRe** framework. Notably, how the Cross-correlated Residual Power (CRPS) is constructed, how templates are used to filter the CRPS for BM physics, and finally how the dependence of BM signatures on source parameters are used to infer both the presence of BM signature and general properties of its origin. In Sec. III, we describe a specific type of possible BM signature: a phase shift in the waveform of binary black holes due to a BM effect that scales as a power law of the mass scale of the system. In Sec. IV A and Sec. IV C, we show how the SNR of the CRPS can be used to recover the index of this power law when the BM signature is small and how both the distribution in source and deviation strength determines which region of source parameter space has the most influence on the inference. Finally, in Sec. IV B, we forecast the constraint on the power law index that can be obtained with two Cosmic Explorer-like detector network over a year. We conclude in Sec. V.

## II. SCORE FRAMEWORK

### A. Beyond Model deviations

In this section, we review the **SCoRe** framework. We start by defining the strain data  $d$

$$d(t) = s(t) + n(t), \quad (1)$$

where  $s(t)$  is the strain caused by the GW signal, while  $n(t)$  is the noise in the detector. In the absence of noise and presence of a signal, the measured strain  $d(t)$  converges to the signal  $s(t)$ . The residual data  $r(t; \theta)$  is ob-

tained by subtracting a model  $m(\theta)^2$ , evaluated at source parameters  $\theta$ , from the data:

$$r(t; \theta) \equiv d(t) - m(t; \theta). \quad (2)$$

The residual data contains noise, the difference between the model at  $\theta$  and at the true parameters  $\theta_T$ , and the BM signature  $\delta$ :

$$r(t; \theta) = m(t; \theta_T) - m(t; \theta) + \delta(t) + n(t). \quad (3)$$

When using the Maximum Likelihood Estimator (MLE)  $\theta = \theta_{\text{MLE}}$ , the bias  $\Delta m(t) \equiv m(t; \theta_T) - m(t; \theta)$  is due to noise and any degeneracy between the BM signature and the model<sup>3</sup>. This is shown in Fig. 1, where both  $\delta$  and  $n$  cause the MLE to be different from the true parameters. In this work, we define the BM signature as  $s - m(\theta_T)$ . If one considers the bias due to degeneracy between the model and the BM signature as part of the BM signature, then the BM signature is  $\delta = s - m(\theta_{\text{MLE}})$ , and the formalism described below remains the same.

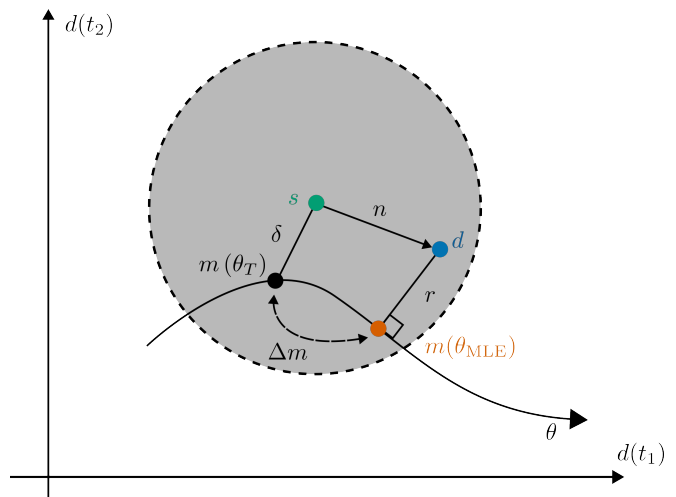


FIG. 1. Geometric illustration of how the data  $d$  arises from the signal  $s$  and the noise  $n$ . If some unmodelled physics is present, the data converges to the BM signature  $\delta$  in the absence of noise. Both the noise and the BM signature cause the MLE of the source parameters,  $\theta_{\text{MLE}}$ , to differ from the true parameters  $\theta_T$ . The residual  $r$  is the difference between the data and the model. The shaded area represents the probability distribution of the noise (where the noise may take the signal to the data with a certain level of probability).

<sup>2</sup> It is important to note that in general the true signal in the data  $s(t)$  can be unknown and differ from the model used in the analysis  $m(t)$ . This is discussed in more detail in the later part of this section.

<sup>3</sup> The bias  $\Delta\theta^i$  on the set of parameters  $\theta^i$ , in the limit of high SNR, is given by  $\Delta\theta^i = (\Gamma^{-1})^{ij} (\partial_j m(\theta_{\text{MLE}}) |n + \delta)$ , where  $\Gamma$  is the Fisher matrix at the MLE, See [46–49].

## B. Cross-correlated Residual Power

A BM signature will be correlated between detectors, whereas noise in different detectors is largely not<sup>4</sup>. This is the principle behind the first step of **SCoRe**. On one hand, the mean time average of the product of BM signatures in two detectors will be non-zero. On the other hand, the mean time average of the product of noise in the detectors will converge to zero as the timescale over which the average is taken increases.

By using this aspect, we define the cross-correlated residual power (CRPS)  $D^{IJ}$  as the mean of the product of the residuals in a pair of detectors  $I$  and  $J$  over a timescale  $\tau$ :

$$D^{IJ}(t; \theta) \equiv \langle r^I r^J \rangle = \frac{1}{\tau(t)} \int_{t-\frac{\tau(t)}{2}}^{t+\frac{\tau(t)}{2}} dt' r^I(t'; \theta) r^J(t' + \Delta t; \theta), \quad (4)$$

where  $\Delta t$  is the time delay between detectors. (The value of  $\Delta t$  may be fixed or jointly inferred/marginalized over as part of  $\theta$  in the analysis.) The important feature of the CRPS is that it converges to  $\delta^I \delta^J$  as  $\tau$  goes to infinity. In analyzing GW waveforms, one usually uses the phase information of the signal. This phase information is lost when taking the CRPS of the data. In the **SCoRe** framework, we instead focus on filtering the power emitted over the timescale  $\tau$ . This is because we aim to remain agnostic about the specific phase evolution of the BM signature, while still capturing any excess or dearth of energy loss that may indicate the presence of a deviation from the SM. Last, we stress that one can still filter out some expected time evolution behavior to test more specifically for certain BM signatures, as we explain in the next section.

## C. Cross-correlated residual power templates

The second step of **SCoRe** filters for the expected time change in the CRPS given a template time function  $Z(t; \theta)$ , which describes the expected time evolution of the excess power due to the BM signature. The templates  $Z(t; \theta)$  are constructed to search for a physically possible signal from the data in a model-independent (or dependent) way<sup>5</sup>. We define the *BM* SNR  $\alpha$  for the

template  $Z(t; \theta)$  as

$$\alpha = \int_{t_s}^{t_e} dt W(t) D^{IJ}(t; \theta) Z(t; \theta), \quad (5)$$

$$\text{where } W(t) \equiv \left( \int_{t_s}^{t_e} dt' N^2(t') Z^2(t') \right)^{-1}.$$

In the above equation,  $t_s$  and  $t_e$  are the start and end times of the signal. The CRPS noise  $N(t)$  is the cross-correlated noise at time  $t$ —the mean ensemble average of the signal in the absence of a BM signature. The weighting function  $W(t)$  is the inverse of the variance of the filtered CRPS, so that  $\alpha$  is the Wiener filter [55] for the template. Note that the match-filtering is performed in time, rather than in frequency. We have assumed that  $\tau$  is greater than the timescale of auto-correlation of the noise. Here, we have chosen the templates  $Z(t; \theta)$  so that their time evolution is solely determined by the SM parameters (while the amplitude/SNR of the template is determined by the BM parameter). The CRPS data,  $D^{IJ}$ , depends on the SM parameters, since the residual is different for different source parameters.

## D. Modelling dependence on source parameters

The third step of **SCoRe** combines the information from different events by modeling how BM signatures in different events depend on the source parameters. We introduce a set of hyperparameters  $\Delta_M$  to describe this dependence across the space of source parameters. These hyperparameters can be inferred from a population of events using Hierarchical Bayesian inference, which we describe in Appendix A. Given a set of observed data  $\{d^I\}_i$  (pairs of data strain for each pair of detectors in the network) for each event  $i$ , we marginalize over the source parameters  $\theta_i$  and the individual event BM signatures  $\delta_i$  to obtain the posterior on  $\Delta_M$ :

$$P(\Delta_M | \{d^I\}_i) \propto \pi(\Delta_M) \prod_i \int d\theta_i \mathcal{L}(\{d^I\}_i | \theta_i, \Delta_M) \pi(\theta_i), \quad (6)$$

where  $P(\Delta_M | \{d^I\}_i)$  is the posterior distribution on the hyperparameters  $\Delta_M$  given the data  $\{d^I\}_i$ ;  $\pi(\Delta_M)$  is the prior on the hyperparameters;  $\mathcal{L}(\{d^I\}_i | \theta_i, \Delta_M)$  is the likelihood of observing the data  $\{d^I\}_i$  given the source parameters  $\theta_i$  and the hyperparameters  $\Delta_M$ ; and  $\pi(\theta_i)$  is the prior on the source parameters for event  $i$ . Refer to Appendix A for the description of the hierarchical Bayesian model.

Since the templates can depend on the source parameters, template choice also determines how  $\alpha$  appears in events with different source parameters. The important question is whether one can take into account this dependence in the recovery of  $\Delta_M$ . We explore this in Appendix B. The crucial point is that the BM SNR  $\alpha$  will capture the dependence on the source parameters  $\theta$

<sup>4</sup> Some sources of noise are correlated between detectors. In particular, correlated noise due to magnetic coupling is expected to impact analysis done with 3G detectors (Einstein Telescope) sensitivity [50–54]. Some of these works also suggest mitigation strategies. We do not concern ourselves with this issue at this time (for simplicity) but note that our framework could also be used to study correlated noise itself as a BM signature.

<sup>5</sup> Examples discussed in [41] include templates looking for a chirp-like behaviour.

regardless of the choice of  $Z(t; \theta)$ , given two conditions: (i) the BM signatures remain small (so only leading order effects are relevant) and (ii) the dependence on the template on the source parameters does not change significantly, which can obscure any deviation due to the BM signature present.

### III. EXAMPLE APPLICATION OF SCORE

In this section, we introduce a model to study the SCoRe framework described in the previous section. The goal is to show that a commonly studied type of BM signature can be recovered using the SCoRe method. We define hyperparameters  $\Delta_M$  which regulate the dependence of the BM signature on chirp mass  $\mathcal{M}_c$  as a decaying power law with index  $D$ . We model the BM signature  $\delta$  induced by this mass-dependent BM signature as a phase shift in the waveform of a binary black hole (BBH) system parameterized by the parameter  $\beta$  given by

$$\beta = \beta_0 \left( \frac{\mathcal{M}_c}{M_0} \right)^{-D}, \quad (7)$$

$$\mathcal{M}_c := (m_1 m_2)^{3/5} (m_1 + m_2)^{-1/5}, \quad (8)$$

where  $\beta_0$  is the value of  $\beta$  at the reference mass scale  $M_0$  (we set  $M_0 = 5 M_\odot$  in the rest of this work), and  $m_1$  and  $m_2$  are the component masses. One could also, for example, consider a change in the amplitude of the waveform, but we focused on the phase shift as it is observed in certain alternatives to GR (see full non-linear solutions obtained in BBH mergers within Einstein-Scalar-Gauss-Bonnet and quartic EFT gravity theories [56, 57]). Indeed certain pipelines, such as the TIGER [58–60] and FTI [61] frameworks, search for deviations in the phase of the waveform when compared to GR [62].

The injected BM signature is then given by

$$\delta(t) = h_{\text{GR}} \left( e^{i\phi_{\text{T}}(t)} - 1 \right), \quad (9)$$

$$\phi_{\text{T}} = -\beta f(t), \quad (10)$$

$$f(t) = \frac{16}{3} \beta c_{\text{Newt}} \frac{M^2}{m_1 m_2} x^{5/2} \times \frac{1 + n_1 x + n_{3/2} x^{3/2} + n_2 x^2 + n_{5/2} x^{5/2} + n_3 x^3}{1 + d_1 x + d_{3/2} x^{3/2}}, \quad (11)$$

$$x := (\hat{\omega}/2)^{2/3}, \quad \hat{\omega} = M \partial_t \phi(t) \quad (12)$$

where  $\phi$  is the phase of the GR (model) waveform and  $M$  is the total mass of the system. We have used the time dependence of the phase described in [63–65], with the parameter  $\beta$  acting as the effective tidal deformability ( $\tilde{\Lambda}$ ). The waveform model  $h_{\text{GR}}$  is the signal predicted by GR. This is the BM waveform  $m = h_{\text{GR}}$  in the formalism of SCoRe. The constants  $c_{\text{Newt}}$ ,  $n_i$ , and  $d_i$  are fitting values given in the above references. This is motivated by the observation that black holes in Effective Field Theories

(EFTs) of gravity described by Eq. 13 (which we describe below) have non-zero tidal Love numbers (e.g. [66]), but in more general terms describes a phase shift that becomes more consequent near merger.

A critical feature of the SCoRe framework is that, although the parameter  $D$  informs on the physics of the BM signature, its value alone does not uniquely determine the source of the BM signature. Several different physical effects could lead to the same value of  $D$ . As hinted above, one possible source of BM signature that would give a scaling of this form is the presence of EFT of gravity effects. A BM signature due to a higher curvature term in the action of gravity is expected to scale inversely with the mass of the binary. Consider the Lagrangian for the EFT of gravity

$$\mathcal{L}_{\text{EFT}} = \frac{1}{16\pi G} \int d^4x \sqrt{-g} (R + l_{\text{UV}}^2 \mathcal{L}_4 + l_{\text{UV}}^4 \mathcal{L}_6 + \dots), \quad (13)$$

where  $l_{\text{UV}}$  is the cutoff length scale of the EFT, and  $\mathcal{L}_n$  are the mass dimension- $n$  operators composed of functional of the Riemann tensor. This framework is described in [67]. The physical effect of each group of operators is suppressed by a factor of  $(l_{\text{UV}}/M)^D$ , where  $M$  is the mass scale of the system and  $D$  depends on  $n$  in some way that can be computed from the form of the operator. Current constraints on the scale  $l_{\text{UV}}$  (for Einstein-scalar-Gauss-Bonnet theory, see [68, 69]) indicate that it must be shorter than the curvature scale of the smallest black holes observed.

The idea that BM effects scale as the mass of the system has previously been used in null tests using post-Newtonian deviation coefficients [39] and ringdown constraints [70, 71]. We stress that this is not the only possible dependence. Another example is an unaccounted object deformability, which changes the quadrupole moment of the system with a degree that increases with the spin of the object. This is notably interesting to distinguish black holes from exotic compact objects (e.g. [8, 72–76]).

We assume the GW source parameters denoted by  $\theta$  (in this analysis we consider the primary and secondary masses  $m_1$  and  $m_2$ , the effective spin  $\chi_{\text{eff}}$ , and the redshift  $z$ ) are distributed according to the phenomenological models found to be consistent with the data in [7, 77, 78]. The most consequent parameters for the analysis are the component masses, the redshift, and the spin of the source. The primary and secondary masses,  $m_1$  and  $m_2$ , are drawn from the Power Law + Gaussian peak model introduced in [79], which models the observed paucity of black holes at low masses, a peak at a mass set by the Pair-Instability Supernova scale, and a power law tail at high masses. The redshift  $z$  is drawn from a distribution inspired by the Madau-Dickinson star formation rate, a phenomenological fit of the star formation rate density of the universe [80], as in [81]. We have used Flat  $\Lambda$ CDM cosmological model in this analysis [82, 83]. The effective spin  $\chi_{\text{eff}}$  is drawn from a Gaussian

distribution with mean  $\mu_\chi$  and standard deviation  $\sigma_\chi$ . These models are summarized in Table I and described in Appendix C.

## IV. RESULTS

### A. CRPS scaling

As described in Sec. IID, the SNR  $\alpha$  carries a dependence on the source parameters in the presence of a BM signature. Notice three effects that determine the dependence of  $\alpha$  on the chirp mass in the toy model from Sec. III. First,  $\alpha$  depends on  $\mathcal{M}_c$  through  $\beta$ , and that dependence is  $\mathcal{M}_c^{-2D}$  to leading order in  $\beta$ . Secondly,  $\alpha$  also depends on the  $\mathcal{M}_c$  through the SM model  $h_{\text{GR}}$ , which gives an additional dependence as  $\mathcal{M}_c^{5/2}$ . This means that the expected scaling of  $\alpha$  with  $\mathcal{M}_c$  is  $\mathcal{M}_c^{5/2-2D}$ . Finally, the other source parameters on which  $\alpha$  does not explicitly depend will also affect the BM SNR. As the source parameters of the GW events arise from an astrophysical population of parameters described in Table I which control the SNR of the event, we expect a spread in the value of  $\alpha$  for a given  $\mathcal{M}_c$ .

We illustrate these effects in Fig. 2, where we plotted the optimal BM SNR  $\alpha$  as a function of the chirp mass for an ensemble of  $10^5$  events. The orange line represents the expected scaling of  $\alpha$  with  $\mathcal{M}_c$ . The SNR at reference chirp mass  $M_0$  has been fit (least squares). The dashed green line shows the recovered fit. The distribution in source parameters other than mass causes a Log-Normal spread in the SNR. This is because the source parameters affect the waveform through terms that are multiplied by one another. By the central limit theorem for products of random variables, the distribution of the product of the terms will be Log-Normal.

On the left (right) of Fig 2, the injected scaling is  $D = 3$  ( $D = 6$ ), while the least-squares fit recovers  $D = 2.9$  ( $D = 4.5$ ). The larger discrepancy in the second case is due to the presence of stronger BM signatures at lower masses and higher orders of  $\beta$  becoming relevant<sup>6</sup>. The discrepancy between the injected and recovered scaling, when the signal is large, is due to the presence of next-to-leading order terms in  $\beta$  contributing to the BM SNR Eq. (5). The value of  $\beta$  at which higher than leading order terms become relevant depends on the behavior of  $f(t)$ .

In the low  $\beta$  case where only the leading-order effect is important, the BM SNR scales in a way that can be predicted directly from expecting a power-law, and therefore one can recover the  $D$  without fine-tuning the template  $Z$ . In the case of high  $\beta$ , next-to-leading order terms

must be included in the template to improve the recovery of the scaling, as described in the SCoRe technique [41]. The latter case is less agnostic to the choice of template.

The difference between the high and low  $\beta$  cases is illustrated in more detail in Fig. 3, where, in the first row, we illustrate the SM and BM waveforms for the example event indicated by a red cross in Fig. 2. The event had a luminosity distance of 1.19Mpc and chirp mass of  $8.15M_\odot$ , and the strain shown was projected onto the illustrative New Mexico CE detector. The case on the right corresponds to the steeper power-law  $D = 6$ , and gives  $\beta = 35.3$  for this event, while on the left  $D = 3$  gives  $\beta = 1.16$ . The stronger value of  $\beta$  gives a visually recognizable phase shift in the waveform. The CRPS of the event is plotted for both values of  $\beta$  on the second row of Fig. 3. For the larger value of  $\beta$ , the CRPS surpasses the cross-correlated noise level near the merger. To compute the CRPS in Figs. 2 and 3, we have used  $\tau = 2.44$  ms, corresponding to integrating over 40 time-samples at 16kHz.

### B. Constraints for next-generation network of GW detectors

The last section argued that BM hyperparameters can be recovered from a population of events, given that the BM signature is small in individual events. We now consider how well our example BM model hyperparameter  $D$  can be constrained by a network of GW detectors. We are interested in demonstrating the method in the regime where the SNR of the SM model is high, but much larger than the SNR of the BM signature—where the residual signal is small compared to the SM model. This regime will be relevant for the next-generation detectors, so we consider a network of two CE-like detectors. The same analysis could be repeated for current detectors, especially by using data from already detected events.

We use the Power Spectral Density (PSD) derived from the Amplitude Spectral Density (ASD) for the baseline 40 km CE design [84] and the New South Wales and Idaho locations in [85]. We have used the CE PSD and potential configurations as an illustration of 3G detector capacities, but the analysis could also be performed with an ET-like detector (see for example [86, 87]). As the anticipated sensitivity of both types of detectors is similar, we do not expect the results to differ qualitatively.

In this analysis, the source parameters of GW events are drawn from an astrophysical population model (as described in the Appendix C) with a choice of parameters shown in Table I. Events with optimal match-filtering SNR (computed using the SM waveform  $h_{\text{GR}}$ ) greater than 8 are selected. The likelihood  $\mathcal{L}$  in Eq. 6 is then computed by marginalizing over the source parameters and the BM SNR  $\alpha$ . As we are interested in the precision of the method, we do not compute the full likelihood for each event. Instead, we approximate the likelihood in

<sup>6</sup> This is not related to the different values of  $D$ , but purely to the strength of the deviation in individual events.

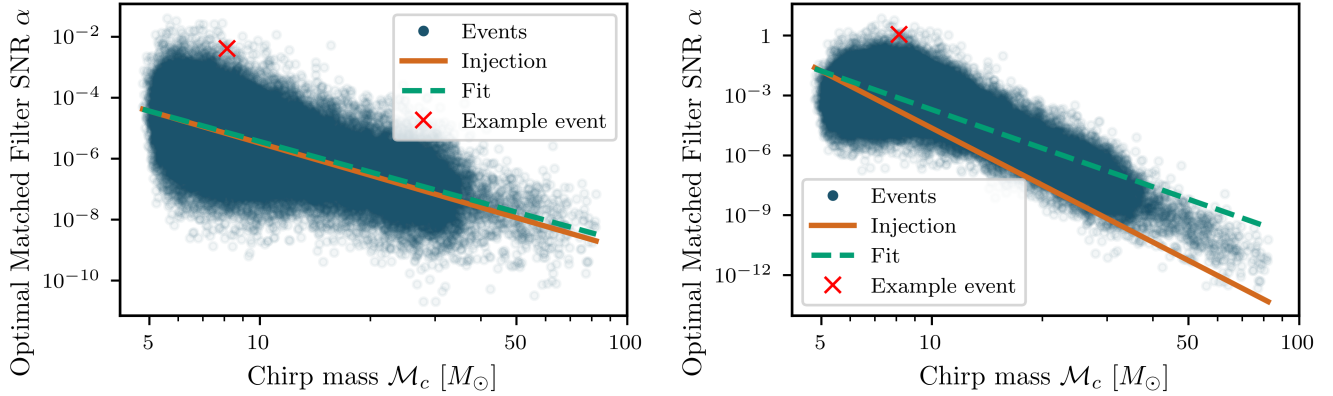


FIG. 2. Optimal BM SNR  $\alpha$  as a function of the chirp mass for an ensemble of  $10^5$  events. The orange line represents the expected scaling of  $\alpha$  with  $\mathcal{M}_c$ . The SNR at reference chirp mass  $M_0$  has been fit (least squares). The dashed green line shows the recovered fit. The distribution in source parameters other than mass causes a Log-Normal spread in the SNR. On the left (right) of the figure, the injected scaling is  $D = 3(6)$  and  $\beta_0 = 5(660)$ , while the least-squares fit recovers  $D = 2.9(4.5)$ . The larger discrepancy in the second case is due to the presence of stronger BM signatures at lower masses as higher orders of  $\beta$  become relevant. The BM and SM waveforms, as well as the CRPS for the event with the SNR indicated by the red cross, are shown in Fig. 3.

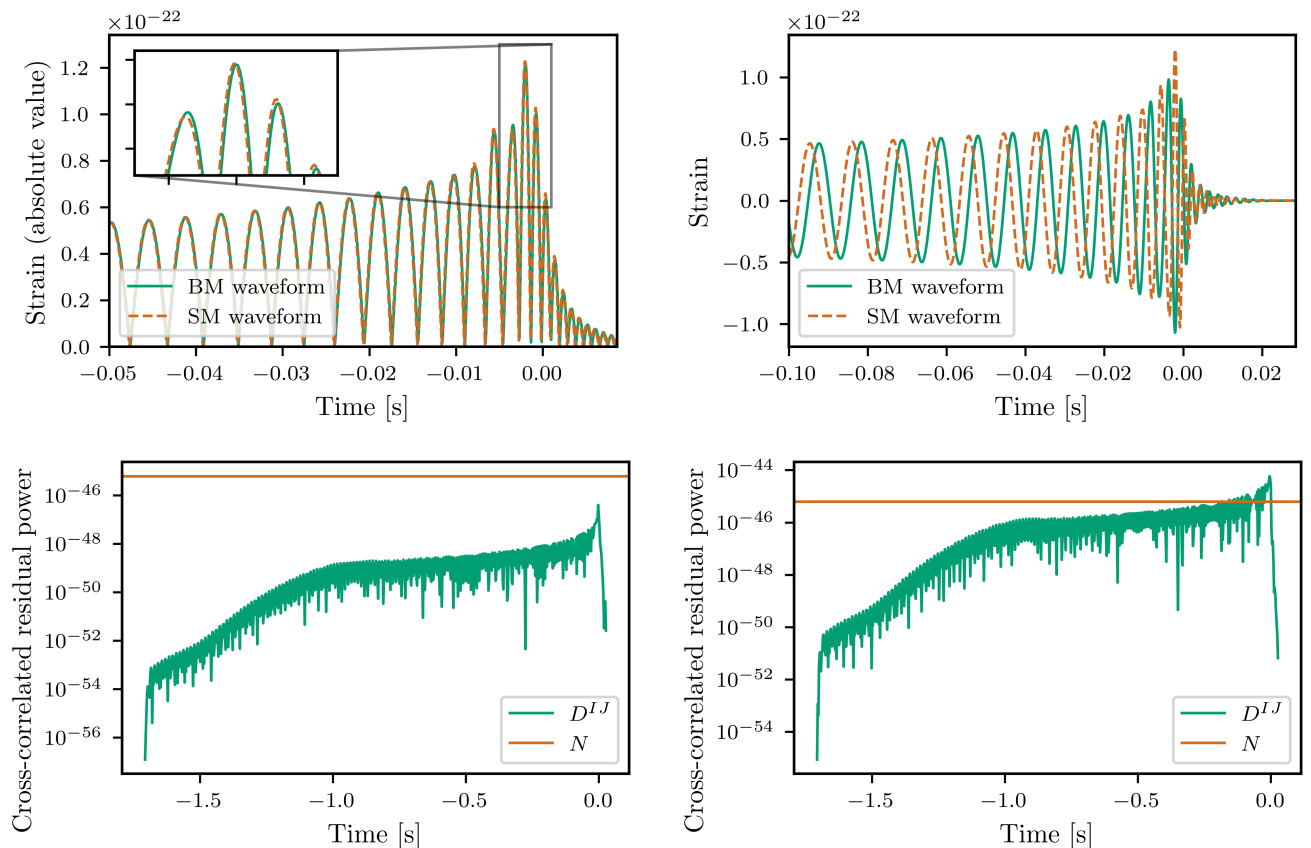


FIG. 3. Top row: SM and BM waveforms for the example event indicated by a red cross in Fig. 2. The event has a luminosity distance of 1.19Mpc and chirp mass of  $8.15M_\odot$ . The strain shown has been projected onto the illustrative New Mexico CE detector. The case on the right corresponds to the steeper power law ( $D = 6$ ), and gives  $\beta = 35.3$  for this event, while on the left  $D = 3$  gives  $\beta = 1.16$ . Bottom row: CRPS of the event, plotted for both values of  $\beta$ . For the larger value of  $\beta$ , the CRPS surpasses the cross-correlated noise level near the merger.

Physical quantity	Model distribution	Model parameters
Redshift Evolution	Madau-Dickinson star formation rate and Flat $\Lambda$ CDM cosmological model	$\gamma = 2.7, \kappa = 2.9, z_p = 1.9,$ $\Omega_M = 0.3, \Omega_\Lambda = 0.7, H_0 = 70 \text{ km/s/Mpc}$
Primary mass	Power law + Gaussian peak	$\lambda = 0.04, \alpha = 3.4, m_{\min} = 5M_\odot, m_{\max} = 100M_\odot,$ $\mu_m = 35M_\odot, \sigma_m = 3.9M_\odot, \delta_m = 4.8$
Secondary mass	Truncated power law	$\beta = 1.3$
Effective spin	Gaussian	$\mu_\chi = 0.06, \sigma_\chi = 0.12$

TABLE I. The astrophysical population parameters and cosmological parameters used in the analysis are given in the table.

$\alpha$  and  $\theta$  as a Gaussian centred on the true values—the values drawn from the population models for  $\theta$  and at zero for  $\alpha$ . The variance of the Gaussian is computed using the Fisher matrix for the best template (the template  $Z(t)$  computed using the injected signal) and the SM waveform model for the event. This yields a lower limit on the variance. See Appendix D for the details of this analysis.

In Fig. 4, we show the posterior on  $D$  and  $\alpha_0$ , the value of  $\alpha$  at the reference chirp mass  $5M_\odot$ . The latter is a measure of the presence of any BM signature in the data. Flat priors were assumed for both parameters, ranging from 2 to 8 for  $D$  and 0 to 1 for  $\alpha_0$ . The left plot shows the upper limit of the 68% credible interval region of the joint posterior. Two features are apparent. First, the constraints loosen as  $D$  increases (generally, for higher mass dimension operators). A sharper power law decay is harder to distinguish from the SM model as the BM signature is weaker for most masses. The constraints tighten as the square root of the number of events. We have assumed a detection rate of  $10^5$  per year [88]. The right plot shows the posterior marginalized over  $D$ . As  $\alpha_0$  is a measure of the presence of any BM signature in the data (and its prior is flat from 0 to 1), the intercept of its posterior with zero gives the Savage Dickey ratio, which is a measure of the evidence for the SM as opposed to any BM signature in the CRPS of the combined data. The zero-intercepts for the different observation times are shown on the x-axis.

We mark the values of the illustrative model for BM deviations with the dashed lines. For example, certain scalar-tensor theories, such as Einstein scalar Gauss-Bonnet gravity predicts  $D = 4$ , while vacuum solutions in Quartic Gravity predict  $D = 6$ . Known physics could also give rise to BM signatures scaling if not accounted for in waveform models. For example, eccentricity effects would give  $D = 5/6$  [89, 90]. Although this was not included in our prior, we note that this effect could potentially be better constrained than the integer values of  $D$  corresponding to EFT operators. We note that, although scaling may be recovered or constrained using this method, it is not possible to distinguish between different models giving the same scaling.

### C. Mass range influence on inference

The results presented in the previous section combine the information from events of all source parameters, particularly masses. In the specific example for which we demonstrated the method, the strength of the BM signature decreases with increasing source mass. At the same time, due to the Power-Law + Gaussian mass distribution and GW selection effects<sup>7</sup>, only a few lighter masses are detectable. As a result, the strongest BM signals may be evident in only a few sources and thus not contribute significantly to the constraints.

To illustrate these two effects and how they impact the influence different mass ranges have on the inference of  $D$ , we consider the posterior on  $D$  obtained from considering only events with a chirp mass within a window of width  $\delta\mathcal{M}_c = 2$ . To focus on the effect of the mass distribution and the variation of SNR with mass, we make three assumptions for the purpose of efficiently computing the posteriors Eq. (6), (i) we assume that the SM source parameters are known exactly, (ii) that the SNR of the BM signature depends only on the chirp mass, and (iii) we are in the limit of a large number of events (as expected from the next generation detectors). The computation of the posterior using these assumptions is described in Appendix E. For the BM signal, we inject an optimal BM SNR  $\alpha$  given by a power law in the chirp mass  $\alpha = \alpha_0 (\mathcal{M}_c/5M_\odot)^{\frac{5}{2}-2D}$ , where  $\alpha_0$  is known exactly and set to  $10^{-38}$ .

In Fig. 5, the blue intensity shows the value of the posterior  $P(D|\{d^I\}_i)$  computed for events with chirp mass within  $[\mathcal{M}_c - \delta\mathcal{M}_c, \mathcal{M}_c + \delta\mathcal{M}_c]$  (this is not a joint posterior, as each value of the x-axis has its own posterior—in the same fashion as a violin plot). The white lines show the upper and lower limits of the 68% (solid) and 95% (dashed) credible intervals change for different mass ranges. The shorter the credible interval, the tighter the

<sup>7</sup> The fraction of lighter mass sources over the high mass sources detectable up to high redshift (and hence over a larger cosmic volume) is less.

<sup>8</sup> The value of  $\alpha_0$  for an actual BM signature would be set by the template used to filter the CRPS and the noise properties of the detector network.



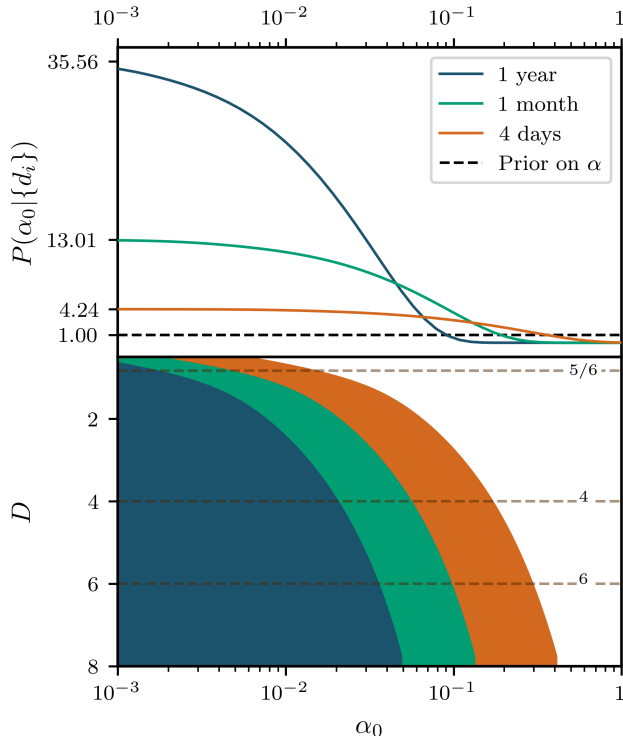


FIG. 4. Posterior on  $D$  and  $\alpha_0$  for a network of two CE-like detectors. The lower plot shows the one  $\sigma$  credible region of the joint posterior for different observation times (assuming a detection rate of  $10^5$  per year). The dashed lines mark the values of the illustrative model for BM deviations. For example, certain scalar-tensor theories give  $D = 4$ , while vacuum solutions in Quartic Gravity give  $D = 6$ . Unaccounted eccentricity effects would give  $D = 5/6$ . The constraints loosen as  $D$  increases and tighten as the square root of observation time (the number of events). The upper plot shows the posterior marginalized over  $D$ . In the absence of BM signatures,  $\alpha_0 = 0$ , and the prior on  $\alpha_0$  is flat from 0 to 1. For these two reasons, the value of the marginalized posterior at zero is a measure of the evidence for the SM as opposed to any BM signature in the CRPS of the combined data (the Savage Dickey ratio).

constraints on  $D$ . To display the two factors affecting the inference, we overlay the injected power law as the orange line corresponding to the right axis. The mass distribution is shown in the middle plot. In the upper (lower) plot, the injected  $D = 4$  ( $\frac{5}{6}$ ). The total number of events in each plot is set so that the tightest constraints are visually comparable (it is set to  $10^{10}$  ( $3 \times 10^7$ ) for the upper (lower) plot). Changing the total number of events would move the constraints in the same proportion across all mass ranges.

The salient point of Fig. 5 is that different mass ranges become more or less informative depending on the scaling  $D$ . In the case of a steeply decaying power law (with  $D = 4$ ), low masses are significantly more informative than higher masses regardless of relative abundance. In

the upper plot, the constraints on  $D$  are shallowest at the lowest chirp masses and then increase with mass. Note the slight convexity of the upper constraints around the PISN peak of the mass distribution ( $\mathcal{M}_c \approx 35M_\odot$ ). As the power law becomes shallower or even increasing (for any  $D > 5/4$ ), the influence of different mass ranges becomes more dominated by the mass distribution. In the lower plot, where we injected  $D = \frac{5}{6}$ , the constraints are tightest at the initial mass peak ( $\mathcal{M}_c \approx 10M_\odot$ ) and at the PISN peak. The lowest mass ranges are not the most informative. In both cases, the decaying power law in the mass distribution means that the constraints on  $D$  are weakened at higher masses<sup>9</sup>.

## V. FINAL WORDS

Whether due to new physics or simply to the complexity of the emission of GWs, our waveform models may not fully capture GW signals in the real data given the sensitivity detectors can reach in the future. This is particularly true as the SNR and sheer number of detected GW events increase with upgrades and new detectors. At the same time, this increase in available data opens the way for more data-driven approaches that do not rely on specific models of BM signatures. A particularly useful feature of BM signatures that can be probed with more data is that some depend on the GW source properties.

In this work, we explored the combination of two such data-driven approaches that can capture any GW source-dependent BM signatures in a model-independent way. Using a novel BM search technique SCoRe [41], we show that one can make an inference of any BM signal by taking into account the dependence on the GW source properties. The cross-correlation of residual which is used in SCoRe allows to distinguish the signal from noise without any specific model assumptions and search for source parameter-dependent BM physics or systematic.

As an illustration, we used a deviation scaling inversely with chirp mass (motivated by EFT of gravity arguments) appearing as a phase shift in the waveform (e.g. [67, 91, 92]). We showed that the index of the power law scaling could be recovered using next-generation GW detectors. We note that while extracting such scaling would not allow one to distinguish between specific models (e.g. specific extensions of GR) will constrain sub-families that are consistent. Further analysis then, with deeper knowledge of specific deviations in particular theories would enable further scrutiny. In Sec. IV B, we forecast the constraints that a network of two CE-like detectors could place on the power-law index with up to one year of observation time. Further, since the variation of the deviation can depend on source parameters

<sup>9</sup> There is a subtle increase in the mass distribution at  $\mathcal{M}_c \approx 50M_\odot$  due to asperities in the KDE estimate (see Appendix E).



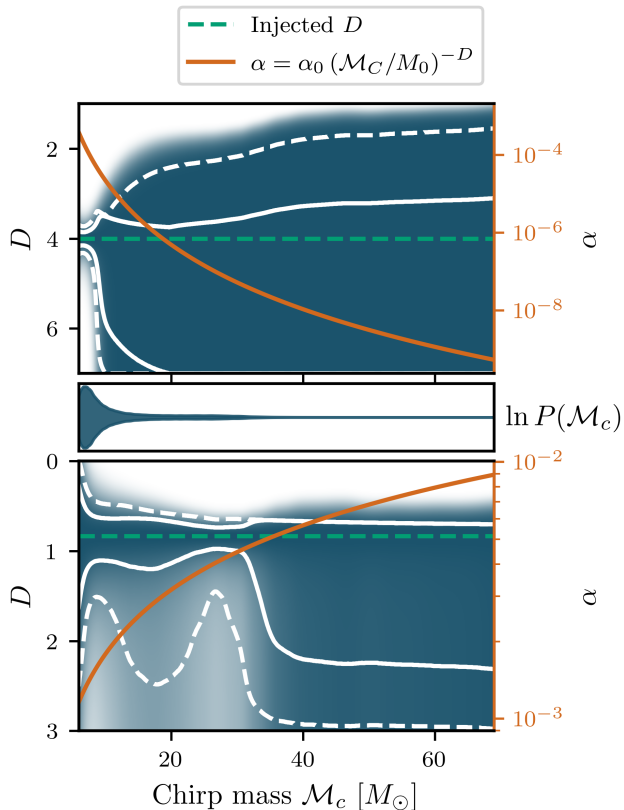


FIG. 5. Posterior on  $D$  for different mass ranges (we assume the value of  $\alpha_0$  is known exactly in the inference). The blue intensity shows the value of the posterior  $P(D|\{d^I\}_i)$  computed for events with chirp mass within  $[\mathcal{M}_c - \delta\mathcal{M}_c, \mathcal{M}_c + \delta\mathcal{M}_c]$  (each value of the x-axis has its own posterior—in the same fashion as a violin plot). The white lines show the upper and lower limits of the 1 (solid) and 2 (dashed)  $\sigma$  credible intervals change for different mass ranges. The shorter the credible interval, the tighter the constraints on  $D$ . We overlay the injected SNR as the orange line corresponding to the right axis. The mass distribution is shown in the middle plot. In the upper (lower) plot, we injected  $D = 4$  ( $\frac{5}{6}$ ). The total number of events in each plot is set so that the tightest constraints are visually comparable (it is set to  $10^{10}(3 \times 10^7)$  for the upper (lower) plot). For a steeply decaying power law (with  $D = 4$ ), low mass ranges are significantly more informative than higher masses. For shallower or increasing power laws (with  $D > \frac{5}{4}$ ), the mass distribution determines the influence of different mass ranges.

and hence impact the inference, we explored which parts of the parameter space are most informative to find BM signatures. In Sec. IV C, we showed that lower masses are most informative when the underlying deviation steeply decays with chirp mass, while the mass distribution dominates the inference when the deviation is shallower or increasing with mass.

Although a specific model (a deviation scaling inversely with mass scale) is used in this paper to demonstrate the ability of the technique SCoRe to capture a GW source-

dependent signature in the data, it can be applied to any kind of BM signatures ranging from physical effects to unknown waveform systematic. This method can be easily extended to look for new physical effects such as spin-induced quadrupole moments, tidal deformation of neutron stars, and signatures of exotic compact objects. Furthermore, it can be used for discovering any common systematic between different detectors induced due to mis-modeling of waveforms<sup>10</sup>. We plan to explore these in our future work. In summary, this technique SCoRe makes it possible to discover BM signatures in a data-driven way and its application on the current network of GW detectors and in the next-generation detectors will bring new insights into the Universe.

## ACKNOWLEDGMENTS

The authors are thankful to Maximiliano Isi for providing useful comments on the manuscript as a part of the LIGO publication and presentation policy and for useful discussions. The authors also thank Katerina Chatziioannou, Zoheyr Doctor, Reed Essick, and Ma SiZheng for useful discussions. The authors would like to thank the LIGO-Virgo-KAGRA Scientific Collaboration for providing the noise curves. This research has made use of data or software obtained from the Gravitational Wave Open Science Center (gw-openscience.org), a service of LIGO Laboratory, the LIGO Scientific Collaboration, the Virgo Collaboration, and KAGRA. LIGO Laboratory and Advanced LIGO are funded by the United States National Science Foundation (NSF) as well as the Science and Technology Facilities Council (STFC) of the United Kingdom, the Max-Planck-Society (MPS), and the State of Niedersachsen/Germany for support of the construction of Advanced LIGO and construction and operation of the GEO600 detector. Additional support for Advanced LIGO was provided by the Australian Research Council. Virgo is funded, through the European Gravitational Observatory (EGO), by the French Centre National de Recherche Scientifique (CNRS), the Italian Istituto Nazionale di Fisica Nucleare (INFN) and the Dutch Nikhef, with contributions by institutions from Belgium, Germany, Greece, Hungary, Ireland, Japan, Monaco, Poland, Portugal, Spain. The construction and operation of KAGRA are funded by Ministry of Education, Culture, Sports, Science and Technology (MEXT), and Japan Society for the Promotion of Science (JSPS), National Research Foundation (NRF) and Ministry of Science and ICT (MSIT) in Korea, Academia Sinica (AS) and the Ministry of Science and Technology (MoST) in Taiwan. This material is based upon work supported by

<sup>10</sup> In order for their effect on parameter inference to remain below that of statistical errors, in CE-like ground-based detectors, the level of systematic errors should be reduced by 1–3 orders of magnitude [93].

NSF's LIGO Laboratory which is a major facility fully funded by the National Science Foundation. This research was supported in part by a NSERC Discovery Grant and CIFAR (LL), the Simons Foundation through a Simons Bridge for Postdoctoral Fellowships (SM) as well as Perimeter Institute for Theoretical Physics. Research at Perimeter Institute is supported by the Government of Canada through the Department of Innovation, Science and Economic Development Canada and

by the Province of Ontario through the Ministry of Research, Innovation and Science. The work of SM is a part of the `<data|theory> Universe-Lab` which is supported by the TIFR and the Department of Atomic Energy, Government of India. In the analysis done for this paper, we have used the following packages: PYCBC [94], LALSUITE [95], NUMPY [96], SCIPY [97] and MATPLOTLIB [98] with SEABORN [99].

- 
- [1] T. L. S. Collaboration, Advanced LIGO, Classical and Quantum Gravity **32**, 074001 (2015), arxiv:1411.4547 [astro-ph, physics:gr-qc, physics:physics].
- [2] T. V. collaboration, Advanced Virgo: A second-generation interferometric gravitational wave detector, Classical and Quantum Gravity **32**, 024001 (2015).
- [3] K. Somiya and Collaboration), Detector configuration of KAGRA—the Japanese cryogenic gravitational-wave detector, Classical and Quantum Gravity **29**, 124007 (2012).
- [4] The KAGRA Collaboration, Interferometer design of the KAGRA gravitational wave detector, Physical Review D **88**, 043007 (2013).
- [5] T. Akutsu and et al., Overview of KAGRA: Detector design and construction history, Progress of Theoretical and Experimental Physics **2021**, 05A101 (2021).
- [6] B. P. Abbott *et al.* (LIGO Scientific Collaboration), Constraints on the Cosmic Expansion History from GWTC-3, The Astrophysical Journal **949**, 76 (2023).
- [7] Abbott *et al.* (LIGO Scientific Collaboration), Population of Merging Compact Binaries Inferred Using Gravitational Waves through GWTC-3, Physical Review X **13**, 011048 (2023).
- [8] B. P. Abbott *et al.* (LIGO Scientific, Virgo and KAGRA Collaborations), Tests of General Relativity with GWTC-3 (2021), arXiv:2112.06861 [astro-ph, physics:gr-qc, physics:hep-th].
- [9] N. Yunes, K. Yagi, and F. Pretorius, Theoretical Physics Implications of the Binary Black-Hole Mergers GW150914 and GW151226, Phys. Rev. D **94**, 084002 (2016), arXiv:1603.08955 [gr-qc].
- [10] C. D. Capano, I. Tews, S. M. Brown, B. Margalit, S. De, S. Kumar, D. A. Brown, B. Krishnan, and S. Reddy, Stringent constraints on neutron-star radii from multimessenger observations and nuclear theory, Nature Astron. **4**, 625 (2020), arXiv:1908.10352 [astro-ph.HE].
- [11] I. Mandel and F. S. Broekgaarden, Rates of compact object coalescences, Living Rev. Rel. **25**, 1 (2022), arXiv:2107.14239 [astro-ph.HE].
- [12] D. A. Godzieba, D. Radice, and S. Bernuzzi, On the maximum mass of neutron stars and GW190814, Astrophys. J. **908**, 122 (2021), arXiv:2007.10999 [astro-ph.HE].
- [13] S. Klimenko, S. Mohanty, M. Rakhmanov, and G. Mitselmakher, Constraint likelihood analysis for a network of gravitational wave detectors, Physical Review D **72**, 122002 (2005).
- [14] S. Klimenko, S. Mohanty, M. Rakhmanov, and G. Mitselmakher, Constraint likelihood method: Generalization for colored noise., Journal of Physics: Conference Series **32**, 12 (2006).
- [15] S. Klimenko, G. Vedovato, M. Drago, G. Mazzolo, G. Mitselmakher, C. Pankow, G. Prodi, V. Re, F. Salemi, and I. Yakushin, Localization of gravitational wave sources with networks of advanced detectors, Physical Review D **83**, 102001 (2011).
- [16] S. Klimenko, G. Vedovato, M. Drago, F. Salemi, V. Tiwari, G. A. Prodi, C. Lazzaro, K. Ackley, S. Tiwari, C. F. Da Silva, and G. Mitselmakher, Method for detection and reconstruction of gravitational wave transients with networks of advanced detectors, Physical Review D **93**, 042004 (2016).
- [17] S. Klimenko and G. Mitselmakher, A wavelet method for detection of gravitational wave bursts, Classical and Quantum Gravity **21**, S1819 (2004).
- [18] V. Skliris, M. R. K. Norman, and P. J. Sutton, Real-Time Detection of Unmodelled Gravitational-Wave Transients Using Convolutional Neural Networks (2020).
- [19] B. P. Abbott and et al., Effects of waveform model systematics on the interpretation of GW150914, Classical and Quantum Gravity **34**, 104002 (2017).
- [20] K. Chatziioannou and et al., On the properties of the massive binary black hole merger GW170729, Physical Review D **100**, 104015 (2019).
- [21] A. Gupta *et al.*, Possible Causes of False General Relativity Violations in Gravitational Wave Observations, arXiv: 2405.02197 (2024).
- [22] D. Reitze *et al.*, Cosmic Explorer: The U.S. Contribution to Gravitational-Wave Astronomy beyond LIGO, Bulletin of the AAS **51** (2019).
- [23] M. Punturo *et al.*, The Einstein Telescope: A third-generation gravitational wave observatory, Classical and Quantum Gravity **27**, 194002 (2010).
- [24] *et al.* Maggiore, Science case for the Einstein telescope, Journal of Cosmology and Astroparticle Physics **2020** (03), 050.
- [25] M. Evans and et al., A Horizon Study for Cosmic Explorer: Science, Observatories, and Community (2021), arXiv:2109.09882 [astro-ph, physics:gr-qc].
- [26] LIGO Scientific Collaboration and Virgo Collaboration, GWTC-1: A Gravitational-Wave Transient Catalog of Compact Binary Mergers Observed by LIGO and Virgo during the First and Second Observing Runs, Physical Review X **9**, 031040 (2019).
- [27] LIGO Scientific Collaboration and Virgo Collaboration, GWTC-2: Compact Binary Coalescences Observed by LIGO and Virgo during the First Half of the Third Observing Run, Physical Review X **11**, 021053 (2021).

- [28] LIGO Scientific Collaboration, and KAGRA Collaboration, Virgo Collaboration, GWTC-3: Compact Binary Coalescences Observed by LIGO and Virgo during the Second Part of the Third Observing Run, *Physical Review X* **13**, 041039 (2023).
- [29] The LIGO Scientific Collaboration and the Virgo Collaboration, GWTC-2.1: Deep extended catalog of compact binary coalescences observed by LIGO and Virgo during the first half of the third observing run, *Physical Review D* **109**, 022001 (2024).
- [30] Q. Hu and J. Veitch, Accumulating Errors in Tests of General Relativity with Gravitational Waves: Overlapping Signals and Inaccurate Waveforms, *The Astrophysical Journal* **945**, 103 (2023).
- [31] B. P. Abbott *et al.* (LIGO Scientific and Virgo Collaborations), Tests of General Relativity with GW150914, *Physical Review Letters* **116**, 221101 (2016).
- [32] B. P. Abbott *et al.* (LIGO Scientific and Virgo Collaborations), Tests of general relativity with the binary black hole signals from the LIGO-Virgo catalog GWTC-1, *Physical Review D* **100**, 104036 (2019).
- [33] R. Abbott *et al.* (LIGO Scientific and Virgo Collaborations), Properties and Astrophysical Implications of the 150  $M_{\odot}$  Binary Black Hole Merger GW190521, *The Astrophysical Journal Letters* **900**, L13 (2020).
- [34] A. Zimmerman, C.-J. Haster, and K. Chatziioannou, On combining information from multiple gravitational wave sources, *Physical Review D* **99**, 124044 (2019).
- [35] M. Isi, K. Chatziioannou, and W. M. Farr, Hierarchical test of general relativity with gravitational waves, *Physical Review Letters* **123**, 121101, 1904.08011.
- [36] M. Isi, W. M. Farr, and K. Chatziioannou, Comparing Bayes factors and hierarchical inference for testing general relativity with gravitational waves, *Physical Review D* **106**, 024048 (2022).
- [37] E. Payne, M. Isi, K. Chatziioannou, and W. M. Farr, Fortifying gravitational-wave tests of general relativity against astrophysical assumptions, *Physical Review D* **108**, 124060 (2023).
- [38] R. Magee, M. Isi, E. Payne, K. Chatziioannou, W. M. Farr, G. Pratten, and S. Vitale, Impact of selection biases on tests of general relativity with gravitational-wave inspirals, *Physical Review D* **109**, 023014 (2024).
- [39] E. Payne, M. Isi, K. Chatziioannou, L. Lehner, Y. Chen, and W. M. Farr, The curvature dependence of gravitational-wave tests of General Relativity (2024).
- [40] H. Zhong, M. Isi, K. Chatziioannou, and W. M. Farr, Multidimensional hierarchical tests of general relativity with gravitational waves, *Physical Review D* **110**, 044053 (2024).
- [41] G. Dideron, S. Mukherjee, and L. Lehner, New framework to study unmodeled physics from gravitational wave data, *Phys. Rev. D* **107**, 104023 (2023), arXiv:2209.14321 [gr-qc].
- [42] N. J. Cornish and T. B. Littenberg, Bayeswave: Bayesian inference for gravitational wave bursts and instrument glitches, *Classical and Quantum Gravity* **32**, 135012 (2015).
- [43] T. B. Littenberg and N. J. Cornish, Bayesian inference for spectral estimation of gravitational wave detector noise, *Physical Review D* **91**, 084034 (2015).
- [44] N. J. Cornish, T. B. Littenberg, B. Bécsy, K. Chatziioannou, J. A. Clark, S. Ghonge, and M. Millhouse, BayesWave analysis pipeline in the era of gravitational wave observations, *Physical Review D* **103**, 044006 (2021).
- [45] <https://lscsoft.docs.ligo.org/bayeswave/index.html>.
- [46] É. É. Flanagan and S. A. Hughes, Measuring gravitational waves from binary black hole coalescences. II. The waves' information and its extraction, with and without templates, *Physical Review D* **57**, 4566 (1998).
- [47] M. Miller, Accuracy requirements for the calculation of gravitational waveforms from coalescing compact binaries in numerical relativity, *Physical Review D* **71**, 104016 (2005).
- [48] C. Cutler and J. Harms, Big Bang Observer and the neutron-star-binary subtraction problem, *Physical Review D* **73**, 042001 (2006).
- [49] C. Cutler and M. Vallisneri, LISA detections of massive black hole inspirals: Parameter extraction errors due to inaccurate template waveforms, *Physical Review D* **76**, 104018 (2007).
- [50] Y. Himemoto and A. Taruya, Impact of correlated magnetic noise on the detection of stochastic gravitational waves: Estimation based on a simple analytical model, *Physical Review D* **96**, 022004 (2017).
- [51] Y. Himemoto and A. Taruya, Correlated magnetic noise from anisotropic lightning sources and the detection of stochastic gravitational waves, *Physical Review D* **100**, 082001 (2019).
- [52] K. Janssens, Prospects for an isotropic gravitational wave background detection with Earth-based interferometric detectors and the threat of correlated noise (2023).
- [53] Y. Himemoto, A. Nishizawa, and A. Taruya, Distinguishing a stochastic gravitational-wave signal from correlated noise with joint parameter estimation: Fisher analysis for ground-based detectors, *Physical Review D* **107**, 064055 (2023).
- [54] K. Janssens, G. Boileau, N. Christensen, N. Van Remortel, F. Badaracco, B. Canuel, A. Cardini, A. Contu, M. W. Coughlin, J.-B. Decitre, R. De Rosa, M. Di Giovanni, D. D'Urso, S. Gaffet, C. Giunchi, J. Harms, S. Koley, V. Mangano, L. Naticchioni, M. Olivieri, F. Paoletti, D. Rozza, D. O. Sabulsky, S. Shani-Kadmiel, and L. Trozzo, Correlated 0.01–40 Hz seismic and Newtonian noise and its impact on future gravitational-wave detectors, *Physical Review D* **109**, 102002 (2024).
- [55] N. Wiener, *Extrapolation, Interpolation, and Smoothing of Stationary Time Series: With Engineering Applications* (The MIT Press, 1949).
- [56] M. Corman, J. L. Ripley, and W. E. East, Nonlinear studies of binary black hole mergers in Einstein-scalar-Gauss-Bonnet gravity, *Phys. Rev. D* **107**, 024014 (2023), arXiv:2210.09235 [gr-qc].
- [57] R. Cayuso, P. Figueras, T. França, and L. Lehner, Self-Consistent Modeling of Gravitational Theories beyond General Relativity, *Phys. Rev. Lett.* **131**, 111403 (2023).
- [58] T. G. F. Li, W. Del Pozzo, S. Vitale, C. Van Den Broeck, M. Agathos, J. Veitch, K. Grover, T. Sidery, R. Sturani, and A. Vecchio, Towards a generic test of the strong field dynamics of general relativity using compact binary coalescence, *Physical Review D* **85**, 082003 (2012).
- [59] M. Agathos, W. Del Pozzo, T. G. F. Li, C. Van Den Broeck, J. Veitch, and S. Vitale, TIGER: A data analysis pipeline for testing the strong-field dynamics of

- general relativity with gravitational wave signals from coalescing compact binaries, *Physical Review D* **89**, 082001 (2014).
- [60] J. Meidam, K. W. Tsang, J. Goldstein, M. Agathos, A. Ghosh, C.-J. Haster, V. Raymond, A. Samajdar, P. Schmidt, R. Smith, K. Blackburn, W. Del Pozzo, S. E. Field, T. Li, M. Pürrer, C. Van Den Broeck, J. Veitch, and S. Vitale, Parametrized tests of the strong-field dynamics of general relativity using gravitational wave signals from coalescing binary black holes: Fast likelihood calculations and sensitivity of the method, *Physical Review D* **97**, 044033 (2018).
- [61] A. K. Mehta, A. Buonanno, R. Cotesta, A. Ghosh, N. Sennett, and J. Steinhoff, Tests of general relativity with gravitational-wave observations using a flexible theory-independent method, *Physical Review D* **107**, 044020 (2023).
- [62] E. M. Sanger, S. Roy, M. Agathos, O. Birnholtz, A. Buonanno, T. Dietrich, M. Haney, F.-L. Julie, G. Pratten, J. Steinhoff, C. V. D. Broeck, S. Biscoveanu, P. Char, A. Heffernan, P. Joshi, A. Kedia, R. M. S. Schofield, M. Trevor, and M. Zevin, Tests of General Relativity with GW230529: A neutron star merging with a lower mass-gap compact object (2024).
- [63] T. Dietrich, S. Khan, R. Dudi, S. J. Kapadia, P. Kumar, A. Nagar, F. Ohme, F. Pannarale, A. Samajdar, S. Bernuzzi, G. Carullo, W. Del Pozzo, M. Haney, C. Markakis, M. Puerrer, G. Riemenschneider, Y. E. Setyawati, K. W. Tsang, and C. V. D. Broeck, Matter imprints in waveform models for neutron star binaries: Tidal and self-spin effects, *Physical Review D* **99**, 024029 (2019), arXiv:1804.02235 [astro-ph, physics:gr-qc].
- [64] T. Dietrich, A. Samajdar, S. Khan, N. K. Johnson-McDaniel, R. Dudi, and W. Tichy, Improving the NR-Tidal model for binary neutron star systems, *Physical Review D* **100**, 044003 (2019).
- [65] M. Colleoni, F. A. R. Vidal, N. K. Johnson-McDaniel, T. Dietrich, M. Haney, and G. Pratten, IMRPhenomXP\_NRTidalv2: An improved frequency-domain precessing binary neutron star waveform model (2023), arXiv:2311.15978 [astro-ph, physics:gr-qc].
- [66] V. Cardoso, M. Kimura, A. Maselli, and L. Santore, Black holes in an Effective Field Theory extension of GR, *Physical Review Letters* **121**, 251105 (2018), arXiv:1808.08962 [astro-ph, physics:gr-qc, physics:hep-ph, physics:hep-th].
- [67] S. Endlich, V. Gorbenko, J. Huang, and L. Santore, An effective formalism for testing extensions to General Relativity with gravitational waves, *Journal of High Energy Physics* **2017**, 122 (2017), arXiv:1704.01590 [astro-ph, physics:gr-qc, physics:hep-ph, physics:hep-th].
- [68] Z. Lyu, N. Jiang, and K. Yagi, Constraints on Einstein-dilation-Gauss-Bonnet gravity from Black Hole-Neutron Star Gravitational Wave Events, *Physical Review D* **105**, 064001 (2022), arXiv:2201.02543 [astro-ph, physics:gr-qc].
- [69] S. E. Perkins, R. Nair, H. O. Silva, and N. Yunes, Improved gravitational-wave constraints on higher-order curvature theories of gravity, *Physical Review D* **104**, 024060 (2021), arXiv:2104.11189.
- [70] G. Carullo, Enhancing modified gravity detection from gravitational-wave observations using the parametrized ringdown spin expansion coefficients formalism, *Physical Review D* **103**, 124043 (2021).
- [71] A. Maselli, S. Yi, L. Pierini, V. Vellucci, L. Reali, L. Gualtieri, and E. Berti, Black hole spectroscopy beyond Kerr: Agnostic and theory-based tests with next-generation interferometers, *Physical Review D* **109**, 064060 (2024).
- [72] F. D. Ryan, Gravitational waves from the inspiral of a compact object into a massive, axisymmetric body with arbitrary multipole moments, *Physical Review D* **52**, 5707 (1995).
- [73] E. Poisson, Gravitational waves from inspiraling compact binaries: The quadrupole-moment term, *Physical Review D* **57**, 5287 (1998).
- [74] W. G. Laarakkers and E. Poisson, Quadrupole Moments of Rotating Neutron Stars, *The Astrophysical Journal* **512**, 282 (1999).
- [75] N. V. Krishnendu, K. G. Arun, and C. K. Mishra, Testing the Binary Black Hole Nature of a Compact Binary Coalescence, *Physical Review Letters* **119**, 091101 (2017).
- [76] Z. Lyu, M. LaHaye, H. Yang, and B. Bonga, Probing spin-induced quadrupole moments in precessing compact binaries, *Phys. Rev. D* **109**, 064081 (2024), arXiv:2308.09032 [gr-qc].
- [77] B. P. Abbott and et al., Binary Black Hole Population Properties Inferred from the First and Second Observing Runs of Advanced LIGO and Advanced Virgo, *The Astrophysical Journal Letters* **882**, L24 (2019).
- [78] R. Abbott and others, Population Properties of Compact Objects from the Second LIGO-Virgo Gravitational-Wave Transient Catalog, *The Astrophysical Journal Letters* **913**, L7 (2021).
- [79] C. Talbot and E. Thrane, Measuring the Binary Black Hole Mass Spectrum with an Astrophysically Motivated Parameterization, *The Astrophysical Journal* **856**, 173 (2018).
- [80] P. Madau and M. Dickinson, Cosmic Star-Formation History, *Annual Review of Astronomy and Astrophysics* **52**, 415 (2014).
- [81] M. Fishbach, D. E. Holz, and W. M. Farr, Does the Black Hole Merger Rate Evolve with Redshift?, *The Astrophysical Journal Letters* **863**, L41 (2018).
- [82] E. Komatsu, K. M. Smith, J. Dunkley, C. L. Bennett, B. Gold, G. Hinshaw, N. Jarosik, D. Larson, M. R. Nolta, L. Page, D. N. Spergel, M. Halpern, R. S. Hill, A. Kogut, M. Limon, S. S. Meyer, N. Odegard, G. S. Tucker, J. L. Weiland, E. Wollack, and E. L. Wright, Seven-year Wilkinson Microwave Anisotropy Probe (WMAP) Observations: Cosmological Interpretation, *ApJS* **192**, 18 (2011), arXiv:1001.4538 [astro-ph.CO].
- [83] N. Aghanim *et al.* (Planck), Planck 2018 results. VI. Cosmological parameters, *Astron. Astrophys.* **641**, A6 (2020), [Erratum: *Astron. Astrophys.* 652, C4 (2021)], arXiv:1807.06209 [astro-ph.CO].
- [84] V. Srivastava, D. Davis, K. Kuns, P. Landry, S. Ballmer, M. Evans, E. D. Hall, J. Read, and B. S. Sathyaprakash, Science-driven Tunable Design of Cosmic Explorer Detectors, *The Astrophysical Journal* **931**, 22 (2022).
- [85] S. Borhanian, GWBENCH: a novel Fisher information package for gravitational-wave benchmarking, *Class. Quant. Grav.* **38**, 175014 (2021), arXiv:2010.15202 [gr-qc].

- [86] S. Hild and et al., Sensitivity studies for third-generation gravitational wave observatories, *Classical and Quantum Gravity* **28**, 094013 (2011).
- [87] M. Branchesi and et al., Science with the Einstein Telescope: A comparison of different designs, *Journal of Cosmology and Astroparticle Physics* **2023** (07), 068.
- [88] T. Regimbau, M. Evans, N. Christensen, E. Katsavounidis, B. Sathyaprakash, and S. Vitale, Digging Deeper: Observing Primordial Gravitational Waves below the Binary-Black-Hole-Produced Stochastic Background, *Physical Review Letters* **118**, 151105 (2017).
- [89] P. Saini, M. Favata, and K. G. Arun, Systematic bias on parametrized tests of general relativity due to neglect of orbital eccentricity, *Physical Review D* **106**, 084031 (2022).
- [90] P. Saini, S. A. Bhat, M. Favata, and K. G. Arun, Eccentricity-induced systematic error on parametrized tests of general relativity: Hierarchical Bayesian inference applied to a binary black hole population, *Physical Review D* **109**, 084056 (2024).
- [91] P. A. Cano, K. Fransen, T. Hertog, and S. Maenaut, Quasinormal modes of rotating black holes in higher-derivative gravity, *Phys. Rev. D* **108**, 124032 (2023), arXiv:2307.07431 [gr-qc].
- [92] L. Bernard, S. Giri, and L. Lehner, The curvature dependence of gravitational-wave tests of general relativity, in preparation (2024).
- [93] M. Pürrer and C.-J. Haster, Gravitational waveform accuracy requirements for future ground-based detectors, *Physical Review Research* **2**, 023151 (2020).
- [94] A. Nitz *et al.*, Gwastro/pycbc: V2.0.2 release of PyCBC, Zenodo (2022).
- [95] LIGO Scientific Collaboration, LIGO Algorithm Library - LALSuite, free software (GPL) (2018).
- [96] C. R. Harris *et al.*, Array programming with NumPy, *Nature* **585**, 357 (2020).
- [97] P. Virtanen *et al.*, SciPy 1.0: Fundamental Algorithms for Scientific Computing in Python, *Nature Methods* **17**, 261 (2020).
- [98] J. D. Hunter, Matplotlib: A 2d graphics environment, *Computing in Science & Engineering* **9**, 90 (2007).
- [99] M. L. Waskom, Seaborn: Statistical data visualization, *Journal of Open Source Software* **6**, 3021 (2021).
- [100] H. Cramér, *Mathematical Methods of Statistics*, Princeton Mathematical Series No. 9 (Princeton university press, Princeton, 1991).
- [101] C. R. Rao, Information and the Accuracy Attainable in the Estimation of Statistical Parameters, in *Breakthroughs in Statistics*, edited by S. Kotz and N. L. Johnson (Springer New York, New York, NY, 1992) pp. 235–247.

## Appendix A: Hierarchical Bayesian Model

In this appendix, we describe the hierarchical Bayesian model used to infer BM hyperparameters from a set of events, as described in [41]. We expect a BM signature to appear differently in different events. Assuming the BM signature is parametrized by a set of parameters  $\alpha$ , the value  $\alpha$  takes in individual events is determined by a set of hyperparameters  $\Delta_M$  (for example, the scale and

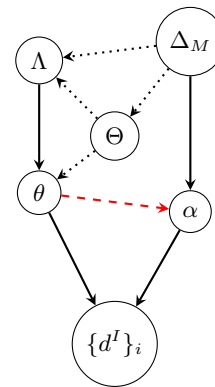


FIG. 6. Schematic representation of the Hierarchical Bayesian model for the inference of a BM signature. The population hyperparameters  $\Lambda$  (e.g PISN mass scale) describe the distribution of source parameters  $\theta$  (e.g. mass and spin) in the population. Likewise, the distribution of BM signature parametrized by  $\alpha$  measured in individual events is described by the hyperparameters  $\Delta_M$ . Cosmological parameters  $\Theta$  could also affect these distributions. By assuming such a hierarchy of dependences and marginalizing over the intermediate parameters, we can recover hyperparameters from a set of event data  $\{d^I\}_i$ . An arrow from node  $A$  to node  $B$  denotes that the prior on  $B$  depends on  $A$ . The physics underlying the BM signature is common to all events and determines the deviation  $\delta$  in individual events according to the parameters  $\Delta_M$ , which should ultimately describe the underlying physics of the BM model (e.g the energy dimension of the leading EFT operator). Although the morphology of the deviation is not known (and must be modeled by the template functions), we expect it to vary consistently with the source parameters  $\theta$  (e.g with a power law dependence on the mass of the BH in our EFT-motivated model). We include this dependence, which corresponds to the red-dashed arrow, in our model. We then attempt to infer the parameters  $\Delta_M$  from the data  $\{d^I\}_i$  by marginalizing over the uncertainties in the intermediate parameters  $\theta$  and  $\alpha$ . The source parameters themselves are distributed according to the population hyperparameters  $\Lambda$ . For the most complete model, we would also include the effect of cosmological models described by parameters  $\Theta$ , which could depend on the BM model and affect the source population.

power law index described in Sec. III). This is shown by an arrow from  $\Delta_M$  to  $\alpha$  in Fig. 6. Similarly, the population hyperparameters  $\Lambda$  (e.g. the Pair-instability Supernova mass scale) describe the distribution of source parameters  $\theta$  (e.g. mass and spin) in the population. The key assumption in our model is that the way  $\alpha$  varies across events is informed by the source parameters  $\theta$ . This is shown by the red dashed arrow in Fig. 6<sup>11</sup>.

This structure can be used to build a hierarchical

<sup>11</sup> For completion, we could also include Cosmological parameters  $\Theta$  in our model. These may affect both the source population parameters  $\theta$  and their distribution (described by  $\Lambda$ ). If the BM signature arises from a modified theory of gravity, the BM

Bayesian model to infer the hyperparameters  $\Delta_M$  from a set of events  $\{d\}_i$ , each labeled by  $i$ . The posterior on the hyperparameters  $\Delta_M$  is given by

$$P(\Delta_M|\{d\}) \propto \mathcal{L}(\{d\}|\Delta_M) \pi(\Delta_M), \quad (\text{A1})$$

where  $\{d\}$  denotes the set of data. Treating the events as independent, the likelihood  $\mathcal{L}(\{d\}|\Delta_M)$  is given by the product of the likelihoods of individual events:

$$\mathcal{L}(\{d\}|\Delta_M) = \prod_i^{N_{\text{obs}}} \prod_{I \neq J}^{N_{\text{det}}} \mathcal{L}(\{d^I, d^J\}_i|\Delta_M, \mathcal{S}), \quad (\text{A2})$$

where each event labelled  $i$  contains a product over pairs of detectors  $I$  and  $J$ . The product is over the  $N_{\text{obs}}$  observed events, and  $\mathcal{S}$ , on the left side of the conditioning bar, denotes that an event has been detected. The selection effects on  $\mathcal{L}(\{d^I, d^J\}_i|\Delta_M, \mathcal{S})$  can be computed taking into account the effects of both  $\theta$  and  $\alpha$  (see [41]). Here, we assume that any event with an optimal match filtering network SNR above 8 is detected. This SNR is computed using the SM template (therefore only taking into account variation in detectability due to  $\theta$ ).

We then marginalize over the source parameters  $\theta$  and the BM signature in individual events ( $\alpha$ ), to obtain the likelihood on the hyperparameters  $\Delta_M$ :

$$\begin{aligned} & \mathcal{L}(\{d^I, d^J\}_i|\Delta_M) \\ &= \int d\theta_i d\alpha_i \mathcal{L}(\{d^I, d^J\}_i|\alpha_i, \theta_i) \pi(\alpha_i|\theta_i, \Delta_M) \pi(\theta_i), \end{aligned} \quad (\text{A3})$$

where we have used the fact that the likelihood only depends on  $\Delta_m$  through  $\alpha_i$  and  $\theta_i$  and that  $\theta_i$  does not depend on  $\Delta_M$ . the prior  $\pi(\alpha|\Delta_M, \theta)$  describes our model for the population of BM signatures. The prior on the event SM parameters  $\theta_i$  is the posterior obtained from fitting the SM waveform.

Note that we marginalize over all the SM parameters, since they may all affect the residual and the templates used to compute the  $\alpha$  parameters. However, not all SM parameters may enter our hierarchical models. Only a subset  $T \in \theta$  may appear in  $\pi(\alpha_i|\theta_i, \Delta_M)$  (for example, in Sec. III  $T = \mathcal{M}_c$ ). In this case, we may set the other parameters, to their MLE value and only marginalize over  $T$ . This is computationally efficient but introduces a bias that scales as the inverse of the SNR squared (in the limit of large SNR).

## Appendix B: Template source parameter dependence

In this appendix, we argue that for small signals and a reasonable choice of template, the hyperparameters

---

hyperparameters may also be related to  $\Theta$ . These relations are shown by the dotted arrows in Fig. 6. In a complete model, all these parameters would be included and inferred or marginalized.

describing the dependence of the BM signature on the source parameters can be recovered from the BM SNR regardless of the choice of template. This is important for agnostic searches for BM signatures of unknown form but whose dependence on the source parameters is modeled.

Consider a CRPS signal  $S(t; \theta, \Delta_M)$  and a template  $Z(t; \theta)$ . We have used the notation to show that the dependence of  $S$  on the source parameters  $\theta$  is determined by the hyperparameters  $\Delta_M$ . If we can factor  $S$  and  $Z$  into a time-dependent and source parameter-dependent part, such that

$$D(t; \theta) = D^\theta(\theta) D^t(t), \quad Z = Z^\theta(\theta) Z^t(t), \quad (\text{B1})$$

then, the BM SNR also factorizes into a time-dependent and source parameter-dependent part:

$$\alpha^\theta \alpha^t = (Z^\theta(\theta) S^\theta(\theta)) \left( \int dt Z^t(t) S^t(t) \right) \quad (\text{B2})$$

and, as we know the template  $Z(t; \theta)$ , we can isolate  $S(\theta)$ . The integral in  $\alpha_T$  acts as a measure of the time match between the model and the signal that is independent of the source parameters.

In our framework, the dependence of  $S$  on the source parameters and BM hyperparameters comes through a waveform-level parameter  $\beta = \beta(\theta, \Delta_M)$  (for example the tidal deformability introduced in Sec. III), which is small when the BM signature is small. This parameter is contained in  $S^\theta$ , and for small BM signatures we can write

$$\alpha \propto (\beta^2 + \mathcal{O}(\beta^3)), \quad (\text{B3})$$

where the leading order is  $\theta^2$  since  $\beta$  parametrised the waveform, which is squared when computing the CRPS.

This property implies that we can recover the BM hyperparameters for any reasonable choice of template, though selecting a template that closely matches the true BM signature will lead to a higher SNR and more sensitive detection.

The factorization of the signal into a time-dependent and source parameter-dependent part relies on the assumption that the dependence of the template on the source parameters does not vary greatly over the signal. As a counter-example, consider choosing  $Z(t; \theta) = \delta(t - \theta)$  or  $Z(t; \theta) = H(t - \theta)$ , where  $\delta$  is the Dirac delta function and  $H$  is the Heaviside step function. These choices may be interesting for studying excess power emitted at specific orbital separations, or continuous losses due to dynamical friction, respectively. In these cases, the template cannot be factorized into a time-dependent and a source parameter dependent part. These templates should therefore not be used for agnostic searches, but are appropriate for specific searches for BM signatures with known time dependence.

In Sec. IV, we used  $Z = S$  to compute the best-case BM SNR. To illustrate that results are not dependent on



this choice, we show, in Fig. B, the BM SNR computed using the agnostic template

$$Z(t; \theta) = \left\langle \frac{d \ln f_I(\theta)}{dt} \frac{d \ln f_J(\theta)}{dt} \right\rangle, \quad (\text{B4})$$

where  $f_I$  and  $f_J$  are the orbital frequencies computed using the SM waveform model in detectors  $I$  and  $J$ . The figure is comparable to the left panel of Fig. 2 (where  $D = 3$  and  $\beta_0 = 5$ ), and shows the BM SNR computed for the same events. The same scaling with chirp mass is recovered, although there is a larger spread in the SNR recovered. The recovered scale ( $\alpha_0$ ) is smaller than when  $Z = S$  since the template and signal are not perfectly matched in time. The decrease is only from  $3.6 \times 10^{-5}$  to  $3.2 \times 10^{-5}$ , as most of the SNR comes from the final stages of the inspiral where the template and signal are well matched.

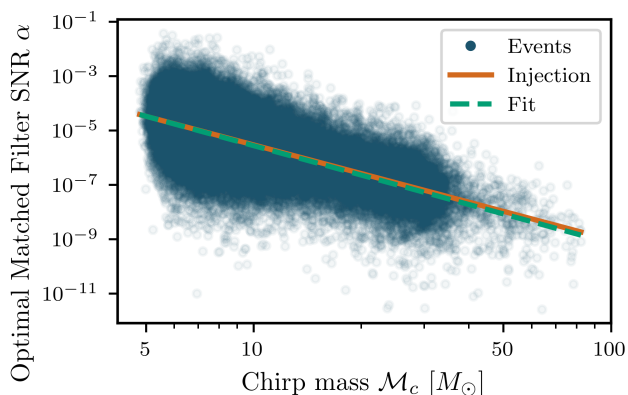


FIG. 7. BM SNR computed using the agnostic, orbital frequency-based template for the same events as in Fig. 2.

### Appendix C: Population models

We sample the source parameters used in our analysis from the following distribution:

$$P(\vec{\theta}) = P(m_1, m_2) P(\chi_{\text{eff}}) P(z) P(\vec{\theta}_{\text{ext}}), \quad (\text{C1})$$

where  $\vec{\theta}_{\text{ext}}$  includes the sky location, the angle between the total angular momentum and the line of sight, the polarisation angle, geocentric time and GW phase at merger. Notably, we assume that all parameters are independent, except for the primary and secondary masses. The samples are obtained from  $P(\vec{\theta}_{\text{GR}})$  by inverse transform sampling. We use uniform distributions for the extrinsic parameters and a Gaussian distribution for the effective spin  $\chi_{\text{eff}}$  with mean 0.06 and standard deviation 0.12 as found in [78].

The form and parameters used for the mass, redshift and spin distributions are described below and summarized in Table I.

### 1. Redshift evolution

We assume that the evolution of the BBH merger rate per co-moving volume  $V_c$  tracks the star formation rate up to some efficiency parameter. For the Star formation rate, we use the fitting function used in [80], giving

$$\frac{dN_{\text{GW}}}{dV_c dt_s} \propto (1+z)^\gamma \frac{1 + (1+z_p)^{-(\gamma+\kappa)}}{1 + \frac{1+z}{1+z_p}^{\gamma+\kappa}}, \quad (\text{C2})$$

with  $\gamma = 2.7$ ,  $\kappa = 2.9$  and  $z_p = 1.9$ . The rate in the source frame can be converted into the merger rate at the detector (per detector time  $t_d$ ) per redshift.

$$\frac{dN_{\text{GW}}}{dz dt_d} = \frac{1}{1+z} \frac{dV_c}{dz} \frac{dN_{\text{GW}}}{dz dt_s}, \quad (\text{C3})$$

where the co-moving volume element over a shell of thickness  $dz$  is

$$\frac{dV_c}{dz} = 4\pi \frac{c}{H_0} \frac{(1+z)^2 D_A^2(z)}{E(z)}, \quad (\text{C4})$$

where  $E(z) = \sqrt{(1+z)^3 \Omega_M + \Omega_\Lambda}$  and  $D_A(z)$  is the angular diameter distance. We assume a flat  $\Lambda$ CDM cosmology, with  $H_0 = 70 \text{ km s}^{-1} \text{ Mpc}^{-1}$ ,  $\Omega_\Lambda = 0.7$  and  $\Omega_M = 0.3$ . We show samples drawn from this distribution in Fig. 8, along with the analytical expression.

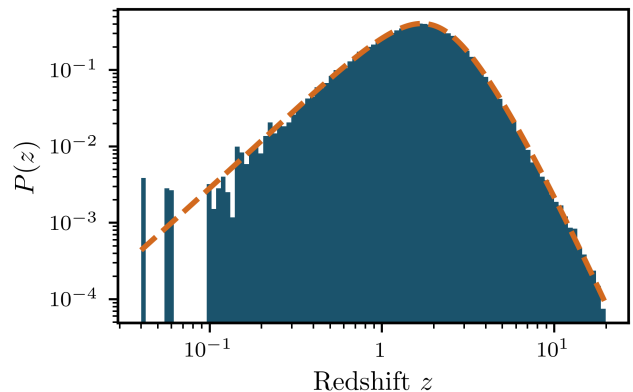


FIG. 8. Samples drawn from the redshift distribution. The analytical expression is shown by the dashed line.

### 2. Mass distribution

We use the Power law + Gaussian peak model from [79] with the best-fit parameters from [7, 78]. This model gives the distribution of the larger, primary mass  $m_1$  as a mixture of a power law and a Gaussian peak:

$$P(m_1 | \Lambda) \quad (\text{C5})$$

$$\propto [(1-\lambda) P_{\text{pow}}(m_1 | \alpha, m_{\text{min}}, m_{\text{max}}) \quad (\text{C6})$$

$$+ \lambda P_{\text{peak}}(m_1 | \mu_m, \sigma_m)] S(m_1, m_{\text{min}}, \delta_m). \quad (\text{C7})$$

where  $P_{\text{pow}}$  is a truncated power law with index  $\alpha$  (we set it to 3.4) and support between  $m_{\text{min}}$  ( $5M_{\odot}$ ) and  $m_{\text{max}}$  ( $100M_{\odot}$ ),  $\lambda$  (0.04) is the fraction of the population that comes from the Gaussian peak,  $P_{\text{peak}}$  is a Gaussian with mean at  $\mu_m$  ( $35M_{\odot}$ ) and  $\sigma_m$  ( $3.9M_{\odot}$ ) standard deviation. A smoothing function  $S$  is applied to avoid discontinuities at lower masses:

$$S(x, m_{\text{min}}, \delta_m) \quad (\text{C8})$$

$$= \left( \exp\left(\frac{\delta_m}{x - m_{\text{min}}} + \frac{\delta_m}{x - m_{\text{min}} - \delta_m}\right) + 1 \right)^{-1}, \quad (\text{C9})$$

for  $m_{\text{min}} \leq m < m_{\text{min}} + \delta_m$ , 0 when  $m < m_{\text{min}}$  and 1 when  $m \geq m_{\text{min}} + \delta_m$ . We use  $\delta_m = 4.8$ . We show samples drawn from this distribution in Fig. 9, along with the analytical expression.

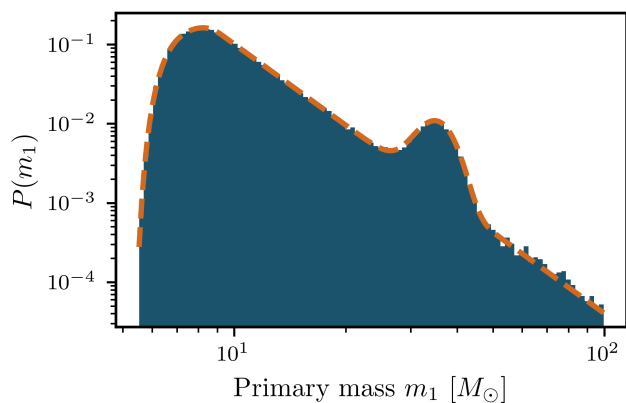


FIG. 9. Samples drawn from the mass distribution. The analytical expression is shown by the dashed line.

The secondary mass is drawn assuming a power law in the mass ratio. This means that the conditional probability from which  $m_2$  is drawn is

$$P(m_2|m_1, m_{\text{min}}, \delta_m) \quad (\text{C10})$$

$$\propto \begin{cases} \left(\frac{m_2}{m_1}\right)^\beta S(m_2, m_{\text{min}}, \delta_m), & m_2 < m_1, \\ 0, & \text{otherwise.} \end{cases} \quad (\text{C11})$$

Equal mass ratios are preferred, and we use  $\beta = 1.3$ .

#### Appendix D: Fisher Analysis

In the analysis carried out in Sec. IV B with the hierarchical Bayesian model described in Appendix A, we need to obtain the likelihood  $\mathcal{L}(d_i|\alpha_i, \theta_i)$  on the SM parameters  $\theta_i$  and the BM parameter  $\alpha_i$  for each event  $i$ . A full computation of this likelihood is expensive and not necessarily informative for a forecast, where we are interested in the general precision of the method. Instead, we approximate it by a Gaussian distribution around the

true values of  $\alpha_i$  and  $\theta_i$ . The values of the BM parameters  $\theta_i$  are drawn from the population models described in Appendix C for each event  $i$ . For our choice of template,  $\alpha_i$  is the optimal match filtering SNR of the CRPS template and is given by  $\alpha = \langle Z|Z \rangle^{-\frac{1}{2}}$ , where

$$\langle A|B \rangle \equiv \int_{t_s}^{t_e} dt W(t) A(t) B(t). \quad (\text{D1})$$

The template function  $Z$  we use is the most accurate CRPS template, and is therefore the best-case scenario for recovery.

We expand the likelihood around the maximum likelihood estimate (MLE) of the parameters and retain only the leading-order term, leaving us with a Gaussian distribution

$$\ln \mathcal{L}(d|\phi) = \ln \mathcal{L}(d_i|\phi_a^{\text{MLE}}) \quad (\text{D2})$$

$$+ \frac{1}{2} (\phi - \phi^{\text{MLE}})^a (\phi - \phi^{\text{MLE}})^b \left( \frac{\partial^2 \ln \mathcal{L}}{\partial \phi^a \partial \phi^b} \right) \Big|_{\phi^{\text{MLE}}} \quad (\text{D3})$$

$$+ \mathcal{O}(\phi^3), \quad (\text{D4})$$

where  $\phi = \{\alpha, \theta\}$ , which includes both the BM SNR and the source parameters. Specific noise realizations will scatter the MLE around the true value of the parameters. However, the expectation value of the MLE with respect to draws of the noise distribution is the true value of the parameters. For a forecast, specific noise realizations are not important, and we can set the MLE to its expectation value. In our analysis, the true values of the SM parameters are drawn from the population models described in Appendix C. For the results in Sec. IV B, the true values of  $\alpha$  are set to 0 for all events.

Assuming the likelihood is Gaussian (which is valid around the MLE in the limit of large SNR), then the inverse of the Fisher matrix,

$$\Gamma_{ab} \equiv -E \left[ \left( \frac{\partial^2 \ln \mathcal{L}}{\partial \phi^a \partial \phi^b} \right) \Big|_{\phi^{\text{MLE}}} \right], \quad (\text{D5})$$

where  $E$  denotes the expectation value over the noise distribution, gives the lower bound on the covariance of the MLE (the Cramér-Rao bound [100, 101]).

In the **SCoRe** framework, the likelihood  $\mathcal{L}(d_i|\phi_i)$  for events labelled  $i$  is computed using both the SM waveform model on the strain data and the BM CRPS model on the residuals obtained. We can compute a Fisher matrix for each of these models, each matrix a  $15+n$  dimensional square matrix, where  $n$  is the number of BM parameters (15 SM parameters and one BM parameter,  $\alpha$ , in our case).

The Fisher matrices for both measurements are combined to obtain the total Fisher matrix:

$$\Gamma_{ab} = \Gamma_{ab}^{\text{SM}} + \Gamma_{ab}^{\text{BM}}. \quad (\text{D6})$$

The total Fisher matrix is then inverted to obtain the covariance matrix of the likelihood  $\mathcal{L}(d_i|\phi_i)$ . In our study,

however, the correlation between the SM and BM parameters is zero, so the Fisher matrix is block diagonal and the likelihood is a product of two independent distributions.

For the SM model  $m(t; \theta)$ , we assume Gaussian, stationary noise and high SNR. With these assumptions, the Fisher matrix takes the simple form:

$$\Gamma_{ab}^{\text{SM}} = 4 \sum_{\text{det}} \Re \int_0^\infty df \frac{1}{S_n(f)} \left( \frac{\partial \tilde{m}}{\partial \phi^a} \right)^* \frac{\partial \tilde{m}}{\partial \phi^b} \quad (\text{D7})$$

where  $S_h(f)$  is the one-sided power spectral density of the strain noise and  $\tilde{m}$  is the Fourier transform of the SM waveform model  $m(t; \theta)$ . The information obtained from each detector is summed over to obtain the network Fisher matrix. Since  $m(t; \theta)$  does not depend on the BM parameters ( $\alpha$ ), the corresponding row and column in the Fisher matrix are set to zero.

The likelihood for the CRPS signal  $D_i^{IJ}$  is given by

$$\ln \mathcal{L}(D^{IJ} | \phi) \propto \langle D^{IJ}(\theta) - Z(\phi) | D^{IJ}(\theta) - Z(\phi) \rangle, \quad (\text{D8})$$

For simplicity, we assume that the value of  $\theta$  used to compute  $D^{IJ}$  are the true values. This will be true in the limit of a small unmodelled signal. With this assumption, the CRPS and template do not depend on the SM parameters. Therefore, the only non-zero element of the Fisher matrix is  $\Gamma_{\alpha\alpha}^{\text{BM}}$ . In the current study, we constructed the templates so that the morphology of the template  $Z$  only depends on the SM parameters, while its SNR for a given event is given by the BM parameter  $\alpha$ . We can then normalize the templates and  $\Gamma_{\alpha\alpha}^{\text{BM}} = 1$ .

Since, in our model,  $\alpha$  only depends on the chirp mass, we marginalize over the other SM parameters. This is simply removing the corresponding rows and columns corresponding to the marginalized parameters in the covariance matrix. The final likelihood is the product of two independent Gaussian distributions):

$$\begin{aligned} \mathcal{L}(\alpha | \mathcal{M}_c) &\propto \exp\left(-\frac{1}{2}(\alpha - \alpha_T(\mathcal{M}_{c,T}))^2\right) \\ &\times \exp\left(-\frac{1}{2}\Gamma_{\mathcal{M}_c \mathcal{M}_c}^{\text{SM}}(\mathcal{M}_c - \mathcal{M}_{c,T})^2\right). \end{aligned} \quad (\text{D9})$$

To obtain the likelihood in  $\Delta_M = \{\alpha_0, D\}$ , we must then compute the integral

$$\begin{aligned} \mathcal{L}(\Delta_M | \{d_i\}) &= \int d\alpha d\mathcal{M}_c \mathcal{L}(d_i | \alpha, \mathcal{M}_c) p(\alpha | \mathcal{M}_c, \Delta_M) \pi(\mathcal{M}_c), \end{aligned} \quad (\text{D10})$$

which marginalizes over all possible mapping of  $\alpha$  and  $\mathcal{M}_c$  to  $\Delta_M$ . We compute this integral numerically for each event.

#### Appendix E: Mass range influence on inference

In this appendix, we derive the posterior computed to obtain Fig 5, which shows the how well different chirp

mass ranges constrain the BM hyperparameter  $D$  variations in the SNR and event distribution across chirp masses. We assume a power law decay in the SNR with the chirp mass, so  $\alpha(D, \mathcal{M}_c) = \alpha_0 (\mathcal{M}_c / 5M_\odot)^{\frac{5}{2} - 2D}$ , and the Power-Law + Gaussian Peak mass distribution described in Appendix C. For simplicity, we assume: that the scale of the power law,  $\alpha_0$ , is known exactly; and that the SM parameters (mass and others) are known exactly and are the same for all events so that the SNR only depends on the chirp mass;

The posterior on  $D$  for  $N$  events and for a set of data  $\{d_i\}$  is given by:

$$P(D | \{d_i\}) \propto \pi(D) \prod_i \mathcal{L}(d_i | D). \quad (\text{E1})$$

If the chirp masses  $\mathcal{M}_c$  of each event are known exactly, we can write:

$$P(D | \{d_i\}) \propto \pi(D) \prod_i \mathcal{L}(d_i | D, \mathcal{M}_c), \quad (\text{E2})$$

where  $\mathcal{L}(d_i | D, \mathcal{M}_c) \propto \exp\left(-\frac{1}{2\sigma_\alpha^2}(\alpha(D, \mathcal{M}_c) - \alpha(D_T, \mathcal{M}_c))^2\right)$ , (E3)

$$\mathcal{L}(d_i | D, \mathcal{M}_c) \propto \exp\left(-\frac{1}{2\sigma_\alpha^2}(\alpha(D, \mathcal{M}_c) - \alpha(D_T, \mathcal{M}_c))^2\right), \quad (\text{E4})$$

where  $\sigma_\alpha = 1$  is the standard deviation of the SNR, and  $D_T$  is the true value of  $D$ . The likelihood can be exponentiated to give:

$$P(D | \{d_i\}) \propto \pi(D) \exp\left(\sum_i^N \ln \mathcal{L}(d_i | D, \mathcal{M}_c)\right). \quad (\text{E5})$$

In the limit of large numbers of events, we approximate the sum with the expectation value of the log-likelihood over the mass range:

$$\begin{aligned} P(D | \{d_i\}) &\propto \pi(D) \exp\left(N \int_{M_{\min}}^{M_{\max}} d\mathcal{M}_c P(\mathcal{M}_c) \ln \mathcal{L}(d | D, \mathcal{M}_c)\right), \end{aligned} \quad (\text{E6})$$

$$\quad (\text{E7})$$

where  $P(\mathcal{M}_c)$  is the mass distribution, including selection effects, and  $M_{\min}$  and  $M_{\max}$  are the minimum and maximum masses in the mass range.

We approximate  $P(\mathcal{M}_c)$  using Kernel Density Estimation on the samples drawn from the full catalog described in Appendix C and discarding samples with match-filtering SNR below 8. In Fig. 10, we show the full event distribution as a function of chirp mass in dark, solid blue; the selected event distribution with the hatched green, and the Kernel Density Estimation in dashed orange.

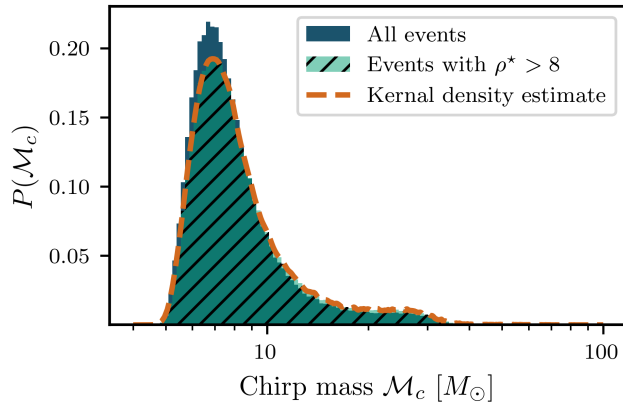


FIG. 10. Kernel Density Estimation of the chirp mass distribution. The full distribution of events, as drawn from the population models described in Appendix C, is shown in solid blue. The distribution of events with match-filtering SNR above 8 is shown in hatched green. We use the Kernel Density Estimation in dashed orange to approximate the mass distribution  $P(\mathcal{M}_c)$  in the posterior computation of Eq. (E6). .